

Linear and Nonlinear Viscoelasticities of Dissociative and Associative Covalent Adaptable Networks: Discrepancies and Limits

Xiang Cui, Nuofei Jiang, Jingyu Shao, Hongdong Zhang, Yuliang Yang, and Ping Tang*



Cite This: *Macromolecules* 2023, 56, 772–784



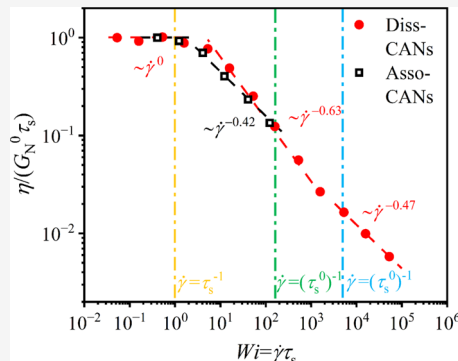
Read Online

ACCESS |

Metrics & More

Article Recommendations

ABSTRACT: Covalent adaptable networks (CANs) can be classified into dissociative (Diss-CANs) and associative (Asso-CANs) networks according to the exchange mechanism of covalent bonds. We simulate the exchange reaction by the hybrid Monte Carlo–molecular dynamics (hybrid MC/MD) algorithm, aiming to discover the connection and difference between Diss-CANs and Asso-CANs in viscoelasticity behavior. In the linear regime, a major difference originating from the cross-linking density is reflected in the pre-exponential factor τ_s^0 of the characteristic relaxation time τ_s . For nonlinear rheology, Diss-CANs show a faster shear thinning behavior under steady shear, while Asso-CANs have a stronger strain hardening under the shear rate start-up. The physics behind the phenomenon results from the different chain conformations and configurations related to the exchange mechanism. Compared with Diss-CANs, the inability for sticker dissociation of Asso-CANs generates a slower relaxation under shear, leading to less chain orientation and tumbling. Meanwhile, we find that multiscale relaxation times obtained from linear viscoelasticity (LVE) can be crucial limits in nonlinear applications for associative polymers (APs). Our work strongly deepens the understanding of APs in terms of both linear and nonlinear viscoelasticities.



1. INTRODUCTION

Covalent adaptable networks (CANs) are covalently cross-linked associative polymers (APs) that possess reversible chemical reactions with the capacity to reshape under external fields. With the strategy of dynamic covalent bonding, traditional thermoplastics and thermosets can be improved to high-strength, reprocessable, and multifunctional materials, widely used in self-healing,^{1,2} shape memory,^{2,3} ion transport^{4,5} materials, etc. Meanwhile, as typical non-Newtonian fluids, the excellent rheological behavior provides support for the theories of APs. The response of CANs is the superposition of both polymer structures and chemical reactions, of which the latter often plays a dominant role. According to the reaction mechanism, they can be further classified into dissociative (Diss-CANs) and associative (Asso-CANs, also known as vitrimers) networks.⁶ The reactions of Diss-CANs take place in terms of sticker dissociation and association, where bond breakage is prior to creation. This allows the formation of intermediates with a number of open stickers and, thus, a loss of cross-links. The rheological behavior of Diss-CANs is very similar to that of typical APs like ionomers. On the contrary, a cross-link of Asso-CANs is only broken when a new covalent bond is formed in the first place, thus maintaining the integrity of the network. Similar to vitreous silica, the macroscopic rheology shows a slower decrease of viscosity with temperature (Arrhenius temperature dependence), which is rarely seen in polymers. Asso-CANs are reported by Leibler⁷ in 2011, and

the name “vitramer” was coined for the first time. As a result, Asso-CANs are novel materials whose viscoelasticity differs from most of the APs.

The dynamics and linear viscoelasticity (LVE) of CANs have been widely reported. Hoy and Fredrickson⁸ investigated the detailed chemical dynamics by creatively using the hybrid Monte Carlo and molecular simulation (hybrid MC/MD) algorithm and identified the kinetically limited and diffusion-limited association behaviors. Rubinstein et al.⁹ studied a simple model of autonomic self-healing of unentangled polymer networks with reversible bonds using scaling theory. Chen et al.^{10,11} examined the thermodynamics and reaction kinetics of dioxaborolane metathesis with and without the byproducts of small molecules. Jiang et al.^{12,13} in our group and Ricarte et al.¹⁴ proposed the sticky Rouse model to describe the LVE of unentangled APs, which can be well applied to CANs. Shao et al.¹⁵ in our group then extended it to a dual-network system. Wu et al.¹⁶ and Perego et al.^{17,18} studied the influence of temperature and kinetic activation

Received: October 16, 2022

Revised: December 19, 2022

Published: February 2, 2023



energy on bond exchange reactions (BERs) of Asso-CANs independently. Olsen et al.¹⁹ studied the walking and hopping diffusion through the intermediate scattering function using Brownian dynamics simulations. However, Elling and Dichtel²⁰ doubted the rationality for demarcating Diss-CANs and Asso-CANs with Arrhenius temperature dependence after surveying the stress relaxation behavior of Diss-CANs. They argued that only a small number of cross-links were broken under typical reprocessing conditions and that Arrhenius-type was still in the majority. Similarly, Montarnal et al.²¹ divided the temperature dependence of viscosity into four regions, of which region II was the fast-dropping stage of viscosity and region I did not have the ability to differentiate. Evans et al.²² found two different regimes of the Arrhenius relationship in the study of polydimethylsiloxane and pointed out the importance of assessing a broad temperature window in probing the dynamic networks of Asso-CANs. Obviously, these arguments collectively specify the indistinct boundary between Diss-CANs and Asso-CANs in LVE.

Nonlinear rheology is more challenging, especially for Asso-CANs. Most of the experimental systems belong to ionic association^{23–30} or hydrogen bond association,^{31–34} and only several theoretical and simulation research studies cover the nonlinearity of CANs. Sing et al.³⁵ computed the fraction of bridged, dangling, and looped chains as a function of associating kinetics by numerically solving Smoluchowski equations of APs modeled as finitely extensible dumbbells. The intertransformation of chain components leads to nonmonotonic flow curves and chain tumbling. Amin and Wang³⁶ applied nonequilibrium molecular dynamics (NEMD) simulations to study the shear and extensional flow behavior of supramolecular polymer networks (SPNs) and their non-associative polymer melt counterparts. In start-up shear, the transient shear viscosities and first normal stress coefficients of both the SPN and melt systems show overshoot behavior, but only the SPNs demonstrate transient strain hardening at high shear rates. In start-up planar extensional flows, all systems demonstrate the characteristic extensional strain hardening behavior, of which the transient extensional viscosities of SPNs undergo a small overshoot.

Here, using molecular simulations, we focus on both the linear and nonlinear viscoelasticities of well-designed networks with different reaction mechanisms. Despite having the same structure, they exhibit huge discrepancies nonlinearly, including the strain hardening of Asso-CANs and the tumbling of Diss-CANs, which are first reported in molecular simulations. Our work not only shows the similarities and differences between Diss-CANs and Asso-CANs but, more importantly, also clarifies the range of application of APs in regard to nonlinear viscoelasticity.

This paper is organized as follows: in Section 2, we present detailed hybrid MC/MD algorithms simulating Asso-CANs and their bond exchange reactions, where the kinetics is verified. In Section 3, the influence of temperature and kinetic activation energy on linear relaxation modulus is discussed as well as the analysis of plateau modulus and terminal relaxation time, where the significance of τ_s^0 is emphasized. In Section 4, a comparison of the two CANs under steady and transient shear is presented, and the change of chain conformation and configuration reveals the connection between microstructure and rheology. Finally, the conclusions are summarized in Section 5.

2. SIMULATION METHODOLOGIES

2.1. Equilibrium Molecular Dynamics (EMD) Simulation of the Networks. Without considering the bond angular potential, we adopt the coarse-grained Kremer–Grest (KG) bead-spring model for representing polymer networks. A total of 500 chains at a length of $N = 50$ are constructed in a cubic periodic box with period $L_i > 2\langle R_{ee} \rangle$ (where $\langle R_{ee} \rangle$ is the mean end-to-end distance), which is at or below the best estimates of the entanglement length $50 \leq N_e \leq 85$.^{37,38} The interaction energy between each unbonded monomer employs the Lennard–Jones (LJ) potential energy U_{LJ}

$$U_{LJ}(r) = 4\epsilon \left[\left(\frac{\sigma}{r} \right)^{12} - \left(\frac{\sigma}{r} \right)^6 + \left(\frac{\sigma}{r_c} \right)^{12} + \left(\frac{\sigma}{r_c} \right)^6 \right] \quad (1)$$

where r is the distance between monomers and the cutoff radius $r_c = 2^{1/6} \sigma_{LJ}$; namely, the pair interaction energy between unbonded monomers is repulsive. The number density of the LJ bead is $\rho = 0.85 / \sigma_{LJ}$. We express all quantities in units of LJ bead diameter σ_{LJ} , intermonomer energy ϵ_{LJ} , and LJ time $\tau_{LJ} = \sqrt{m\sigma_{LJ}^2/\epsilon_{LJ}}$. The covalent bonding between neighbor beads is modeled with the finitely extensible nonlinear elastic (FENE) potential

$$U_{FENE}(r) = -\frac{1}{2} k R_0^2 \ln \left[1 - \left(\frac{r}{R_0} \right)^2 \right] \quad (2)$$

where the spring constant $k = 30 \epsilon_{LJ}/\sigma_{LJ}^2$ and maximum bond length $R_0 = 1.5 \sigma_{LJ}$. All of the simulations are performed using the LAMMPS with canonical (NVT) ensemble under periodic boundary conditions, maintaining the temperature using the Langevin thermostat. Newton's equations of motion are integrated using the velocity Verlet algorithm with a timestep of $\delta t = 0.01 \tau_{LJ}$ at LJ temperatures $T = 0.8–1.6 \epsilon_{LJ}/k_B$, where k_B is the Boltzmann constant. This timestep has been tested as an optimum one and will not lead to chain crossing, which has also been used for the hybrid MC/MD algorithm for the simulation of supramolecular polymer networks (SPNs) by Wang and Likhtman.^{36,39}

We assume four stickers per chain, distributed at $N_i = 3, 18, 33$, and 48 . Each sticker can only additionally bond with one other sticker to avoid phase separation. The premixed chains are cross-linked for 10^8 steps to ensure a fully cross-linked network with about 2.5% loops and no unreacted stickers. This is the prepared initial network for both Diss-CANs and Asso-CANs.

2.2. Simulation of Bond Exchange Reactions. The reversible network of Diss-CANs relies on the dissociation and association of stickers, which is simulated by the breakage and creation of sticky bonds. Following the hybrid MC/MD algorithm first proposed by Hoy and Fredrickson,⁸ we model Diss-CANs in the same way. In this method, the beads move based on the MD governing equations, and the chemical reactions occur in an MC step, in which the probability of bond breakage and creation is calculated independently. For detailed information, please see ref 8.

Inspired by their work, we came up with a similar hybrid MC/MD algorithm describing bond exchange reactions (BERs) for Asso-CANs, as shown in Figure 1. Instead of bond creation and breakage, this chemical reaction can be realized by bond exchange because of the unchanged cross-

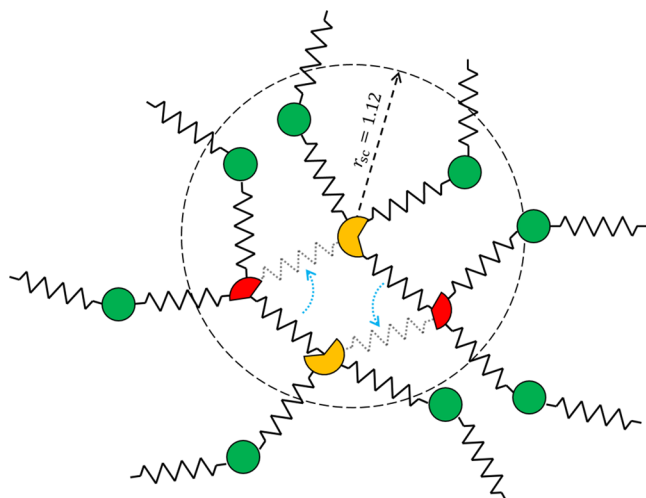
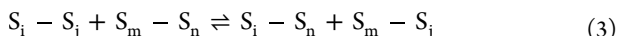


Figure 1. Schematic diagram of the well-defined network and BERs for Asso-CANs. Green circles stand for regular beads, and yellow and red circles represent stickers (the concave–convex shape is just to highlight the association between stickers, which are exactly the same in the simulation). BERs pointed out by the dashed lines and the blue arrows can only happen in the condition that two pairs of bonded stickers are within the r_{sc} circled by the black dashed lines.

linking density. On account of our previous fully cross-linked network, the experimental two-step reaction can be simplified in the simulation by



where S and the subscripts (i, j, m, n) refer to different stickers and the invertible symbol represents a reversible reaction. By ignoring the intermediates, eq 3 describes a one-step bond exchange reaction that happened between four stickers, S_i , S_j , S_m and S_n . The kinetics is also simplified, of which the reaction rates are given by

$$k_+[S_i - S_j][S_m - S_n] = k_-[S_i - S_n][S_m - S_j] \quad (4)$$

where the square brackets stand for concentrations and k_+ and k_- are the forward and backward reaction rates, respectively. With a well-defined network, all stickers are within the network, whether exchanged or not, having the same chemical environment. As a result, the concentration of each sticker remains the same after BERs, and the equilibrium constant is

$$K_{eq} = \frac{k_+}{k_-} = \frac{[S_i - S_n][S_m - S_j]}{[S_i - S_j][S_m - S_n]} \equiv 1 \quad (5)$$

Equation 5 proves that BERs are equiprobable reactions forward and backward, where no change occurs in the structure of the network. According to the Arrhenius model, the reaction rates can be written as

$$k_+ = k_- = A \exp\left(-\frac{E_a^{\text{kin}}}{k_B T}\right) \quad (6)$$

where E_a^{kin} is the reaction kinetic activation energy and A is the prefactor. Equation 6 illustrates that an Arrhenius-type reaction is controlled by kinetics (A) and thermodynamics (E_a^{kin} and T), where $\exp(-E_a^{\text{kin}}/k_B T)$ is in fact the probability or difficulty degree of the reaction. It is noted that eq 6 is a mean-field model ignoring the correlations of stickers, such as concentration fluctuations.

We first focus on the part of thermodynamics. To carry out BERs in the MC simulation, the interaction potential between stickers is defined as

$$U_s(r, H) = -[U_{\text{FENE}}(r) - U_{\text{FENE}}(r_0) - H] \quad (7)$$

where $r_0 \approx 0.96 \sigma_{\text{LJ}}$ is the equilibrium FENE covalent bond length and H is the additional energy barrier. Equation 7 describes the attraction between stickers by U_{FENE} , and the introduction of r_0 , calculated by the combination of U_{LJ} and U_{FENE} , implies that stickers are repulsed by U_{LJ} , vibrating around r_0 . The interaction between stickers only relates to the deviation of r_0 and the energy barrier H . From the point of view of energy, when one of the bonded stickers vibrates far away from the other sufficiently, the FENE potential is able to compensate for the energy barrier; namely, $U_s(r, H) \leq 0$, and the exchange happens. Otherwise, $U_s(r, H) > 0$, and the exchange probability is

$$\Delta = \exp\left[-\frac{U_s(r, H)}{k_B T}\right] \quad (8)$$

When Δ is greater than a random number between 0 and 1, the exchange is accepted. The above MC step violates detailed balance but satisfies the “weaker balance,” which is the necessary and sufficient requirement for MC, as proved by Manousiouthakis and Deem.⁴⁰ Note that there are several differences in simulating Asso-CANs compared with Diss-CANs. First, unlike the binding energy h of Diss-CANs, H is just an additional parameter adjusting the reaction difficulty degree. Second, the simplification of BERs with a one-step reaction is based on a well-defined network with no open stickers, whereas Diss-CANs do not have this limit. At last, stickers of both CANs have a cutoff of $r_{sc} = 1.12 \sigma_{\text{LJ}}$ calculating U_s during MC steps. However, only two bonded or open stickers are considered within r_{sc} for Diss-CANs, while two pairs of bonded stickers are needed within r_{sc} to perform a bond exchange (Figure 1). In other words, besides the energy criterion described in eq 8, the probability of sticker spatial distribution is the other condition that decides whether a BER occurs. As a consequence, the four-body interaction dramatically slows down the kinetics of Asso-CANs, leading to a much smaller viscous flow activation energy E_a^{vis} , calculated from the terminal relaxation time τ_s in Section 3.

We then discuss the part of kinetics in eq 6. Prefactor A is actually the reaction rate (k_+ or k_-) when $E_a^{\text{kin}} \rightarrow 0$ or $T \rightarrow \infty$, which equals the frequency that all stickers attempt BERs once. Hence, A is related to how often a BER occurs, namely, the match of MC and MD timestep τ_{MC} and the probability p_{sc} of two pairs of bonded stickers within r_{sc}

$$A = \frac{p_{sc}}{\tau_{\text{MC}}} \quad (9)$$

where τ_{MC} is defined as

$$\tau_{\text{MC}} = \frac{1}{f_{\text{MC}}} \tau_{\text{mcts}} \quad (10)$$

where τ_{mcts} is the MC timestep and f_{MC} is the fraction of stickers considered in an MC step that is randomly selected. The reason of introducing $f_{\text{MC}} < 1$ is to effectively avoid repeated exchanges of neighboring stickers. We fix the timestep of EMD $\delta t = 0.01 \tau_{\text{LJ}}$, $\tau_{\text{mcts}} = \tau_{\text{LJ}}$, and $f_{\text{MC}} = 0.5$. The p_{sc} in eq 9 can be obtained by the relationship between bond lifetime τ_b

(which is equal to the inverse of reaction rate k_+ or k_-) and BER probability p_{MC} (which is the ratio between the number of successful BERs and attempted BERs, both obtained by simulation output). The bond lifetime τ_b can be calculated by the autocorrelation function (see Section 4.1 for details).

As shown in Figure 2, $p_{sc} \approx 0.15$ is fitted, representing that the probability of four-body interaction is reduced terribly

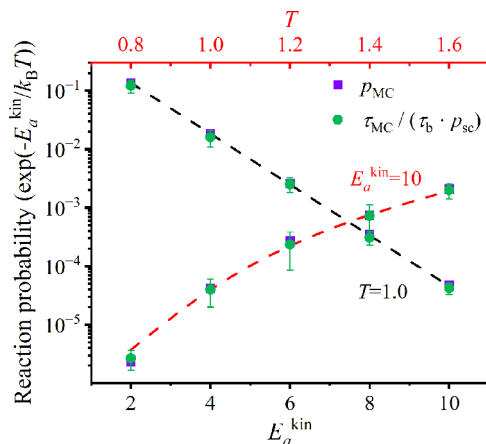


Figure 2. Relationship between reaction probability by eq 6, simulation and fitted, and E_a^{kin} under $T = 1.0 \text{ } k_B T$ or T under $E_a^{\text{kin}} = 10 \epsilon_{\text{LJ}}$. Dashed lines are calculated by $\exp(-E_a^{\text{kin}}/k_B T)$ from eq 6, p_{MC} (■) is the output by the simulation, and $\tau_{MC}/(\tau_b \cdot p_{sc})$ (●) is obtained by fitting $p_{sc} \approx 0.15$.

compared with sticker dissociation and association. The consistency of BER probability p_{MC} in the simulation and Arrhenius reaction probability $\exp(-E_a^{\text{kin}}/k_B T)$ from eq 6 (dashed lines in Figure 2) proves that our MC approach conforms to the chemical reaction in the experiment. The only difference between the simulation and experiment for the fully cross-linked network without open stickers lies in the complete forbiddance of sticker dissociation.

Note that another common simulation method for Asso-CANs is the three-body potential proposed by Sciortino,⁴¹ which is a pure MD algorithm implementing BERs by adding a computationally nonexpensive three-body repulsive potential. This method has been used to simulate stress relaxation,⁴² fragility,⁴³ dynamics,⁴⁴ and self-healing⁴⁵ of Asso-CANs. However, the bonding interaction is mainly based on the harmonic potential, which will generate nonphysical results in the nonlinear regime. Since we are not sure whether replacing it with FENE potential will bring up new problems or not, the hybrid MC/MD algorithm that has been verified by Amin and Wang³⁶ in NEMD is used in this paper.

3.3. NEMD Simulation under Simple Shear. Following the work of nonlinear rheology and dynamics of SPNs by Amin and Wang,³⁶ we perform our NEMD simulation under simple shear with shear rate $\dot{\gamma}$. We use a cubic simulation box and apply the “sliding brick” boundary conditions of Lees and Edwards, which are achieved by simultaneous deformation of the box and the strain. The shear is assumed along the x-axis, and its gradient is along the y-axis. The motion of the beads is controlled by the p-SLLOD equations (note that for steady-state and start-up shear flow as considered herein, the SLLOD

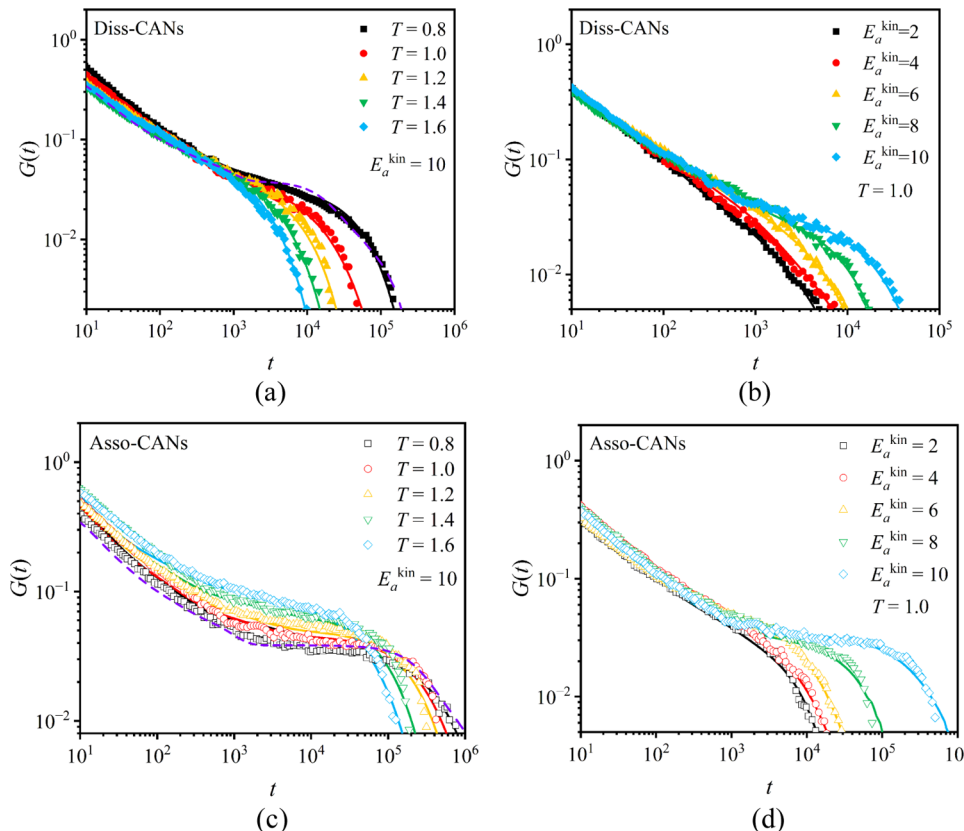


Figure 3. Stress relaxation moduli $G(t)$ under different E_a^{kin} or T values for Diss-CANs (a and b) and Asso-CANs (c and d). Solid lines are multiexponential fittings, and the purple dashed lines in (a) and (c) are calculated by SRM with $\delta = 200$ and 3000 , respectively.

and p-SLLOD algorithms are the same^{46,47} and the p-SLLOD algorithm is the current implementation of NEMD in LAMMPS), which are maintained at a constant temperature of $1.0 k_B T$ using a Nosé–Hoover thermostat. The MD and MC timesteps are chosen in the range of $\delta t = 0.001\text{--}0.005 \tau_{\text{LJ}}$ and $\tau_{\text{mcts}} = 0.1\text{--}0.5 \tau_{\text{LJ}}$, respectively, depending on the strain rate. The kinetic activation energy is fixed at a relatively strong association strength, $E_a^{\text{kin}} = 10 \varepsilon_{\text{LJ}}$.

3. LINEAR VISCOELASTICITY

As mentioned above, Diss-CANs and Asso-CANs have an indistinguishable LVE already reported in many research studies.^{20,21} Nevertheless, our work still starts from here, aiming to prove the reliability of the simulation in Section 2 and dig deeply into multiscale relaxation time of the two networks, especially the prefactor of terminal relaxation time τ_s^0 .

3.1. Influence of Temperature and Kinetic Activation Energy. Before further discussion of relaxation time, we first focus on the influence of temperature ($T = 0.8\text{--}1.6 k_B T$) and kinetic activation energy ($E_a^{\text{kin}} = 2\text{--}10 \varepsilon_{\text{LJ}}$) on linear relaxation modulus $G(t)$, which can be calculated in the simulation from the time correlation functions of off-diagonal components of the stress tensor $\sigma_{\alpha\beta}$ based on the Green–Kubo relationship^{48,49}

$$G(t) = \frac{V}{3k_B T} (\langle \sigma_{xy}(t)\sigma_{xy}(0) \rangle + \langle \sigma_{xz}(t)\sigma_{xz}(0) \rangle + \langle \sigma_{yz}(t)\sigma_{yz}(0) \rangle) \quad (11)$$

where the multitan correlator algorithm⁵⁰ is used to reduce the strong noise in the correlation functions. The simulation time is chosen to be several orders of magnitude larger than our interested longest relaxation time to obtain accurate $G(t)$ behavior, especially at a long time.

As shown in Figure 3, the terminal relaxation time of both Diss-CANs and Asso-CANs shortens as T increases or E_a^{kin} decreases, which is in accordance with exchange kinetics, as in eq 6, namely, faster chemical reactions accelerating the network relaxation. However, the plateau modulus of Asso-CANs is in proportion to T (see Section 3.2) and remains constant with decreasing E_a^{kin} , while that of Diss-CANs keeps declining, vanishing at high T and low E_a^{kin} values. This is a clear sign of cross-linking density loss for Diss-CANs as the reaction goes toward the dissociation direction, and the products are in the majority of intermediates, which is a decisive difference between the two networks in terms of both linear and nonlinear viscoelasticities. Multiexponential fittings are drawn in solid lines in Figure 3, with which the relaxation time of Rouse modes can be obtained.

Our previous work on SRM^{12,15} is an elaborate molecular model, especially for the case of strong association, whose validity has been verified for APs. The purple dashed lines plotted in Figure 3a,c are the relaxation moduli calculated by SRM with relative frictional coefficient $\delta = 200$ and 3000, respectively. The well-fitted data indicates that our simulation corresponds with the theory. As powerful as SRM is, it cannot differentiate between Diss-CANs from Asso-CANs because the cross-linking density is a prerequisite, for which our simulation can be a fine complement.

Having the same segmental motion, $G(t)$ and mean-squared distance (MSD) are consistent at different time scales. According to the scaling relationship, they can be divided

into four regions, as shown in Figure 4. In consideration of the similar LVE, only $G(t)$ of Asso-CANs under $E_a^{\text{kin}} = 10 \varepsilon_{\text{LJ}}$ and T

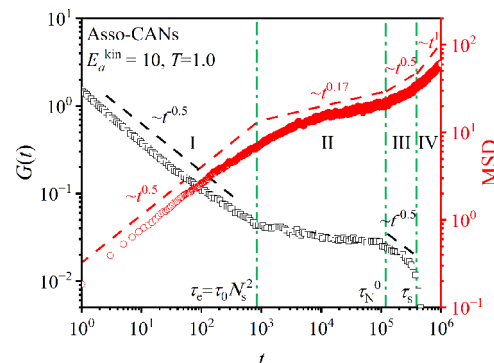


Figure 4. Stress relaxation modulus (\square) and the corresponding MSD (\circ) of Asso-CANs under $E_a^{\text{kin}} = 10 \varepsilon_{\text{LJ}}$ and $T = 1.0 k_B T$. The green dot-dashed lines are the transition points of different scaling relationships.

$= 1.0 k_B T$ is plotted. In region I, $G(t) \sim t^{-0.5}$ and $\text{MSD} \sim t^{0.5}$ are on behalf of Rouse motion and the relaxation time is within $\tau_e = \tau_0 N_s^2$, where τ_e is the time when a chain feels the restriction of the network, τ_0 is the Rouse segment time (calculated by SRM), and N_s is the length of the strand between stickers. In region II, $G(t)$ enters the plateau and MSD slows down significantly when $\tau_e < t < \tau_N^0$, with τ_N^0 being the duration of G_N^0 . This is the area where the network comes into play, and the power law between MSD and t is less than 0.5, where 0.5 is the subdiffusion of the unentangled nonsticky chain. In region III, G_N^0 begins to attenuate until τ_s and, again, $G(t) \sim t^{-0.5}$ and $\text{MSD} \sim t^{0.5}$ are observed, which is equivalent to the Rouse relaxation of chains that ignore nonsticky beads (chains that only consist of stickers). In region IV, when $t > \tau_s$, the network is close to full relaxation and the corresponding diffusion is nearly Fick diffusion with $\text{MSD} \sim t$. The comparison of $G(t)$ and MSD clarifies each size of motion unit and its relaxation time. A quantitative relationship can be found in ref 18.

3.2. Plateau Modulus and Cross-Linking Density. Based on the theory of rubber elasticity, the plateau modulus can be calculated by

$$G_N^0 = \nu k_B T \quad (12)$$

where ν is the number density of cross-linking. Equation 12 indicates that each strand contributes $1 k_B T$ to the total energy. Consequently, G_N^0 of Asso-CANs with conservative cross-links should be in proportion to T , while that of Diss-CANs is related to both ν and T . Figure 5 plots G_N^0 versus T , of which the G_N^0 of Diss-CANs is normalized by ν . It can be seen that all data collapse into eq 12, revealing the entropy elasticity of the network.

Note that, when calculating G_N^0 (and τ_s , see Section 3.3), stress relaxation moduli are converted into storage moduli G' and loss moduli G'' using the relaxation time of Rouse modes obtained from multiexponential fittings. G_N^0 is determined by the value of the minimum of G'' relative to the value of G' at an intermediate frequency.

3.3. Terminal Relaxation Time and Its Prefactor. In APs, the terminal relaxation is controlled by a chemical reaction, which can be written in the Arrhenius form as follows

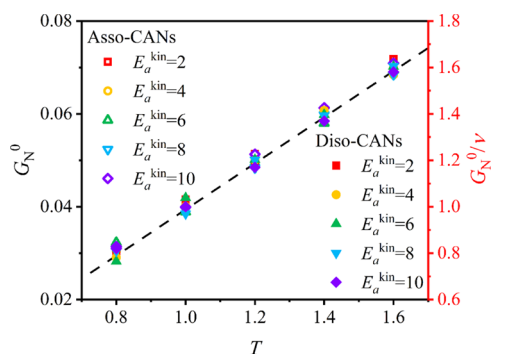


Figure 5. Temperature dependence of G_N^0 for Asso-CANs and normalized G_N^0/v for Diss-CANs. Black dashed lines are calculated by eq 12.

$$\tau_s = \tau_s^0 \exp\left(\frac{E_a^{\text{vis}}}{k_B T}\right) \quad (13)$$

where τ_s^0 is the prefactor and E_a^{vis} is the viscous flow activation energy. Figure 6a,b plots $\tau_s \sim T$ at different E_a^{kin} values for Diss-CANs and Asso-CANs, respectively (τ_s is determined by the crossover of G' and G'' at low frequencies). Except for $T = 0.8$ near topology freezing transition temperature (T_v), all data show $\ln(\tau_s)$ proportional to $1/T$, which is in agreement with eq 13. The slope represents E_a^{vis} of the network. For Diss-CANs, $E_a^{\text{vis}} \approx E_a^{\text{kin}}$ stands up for the argument of a chemical reaction dominating terminal relaxation, while $E_a^{\text{vis}} \approx -E_a^{\text{kin}} \ln(p_{sc})$ for Asso-CANs results from the four-body (bond exchange) interactions (see Section 2 for details).

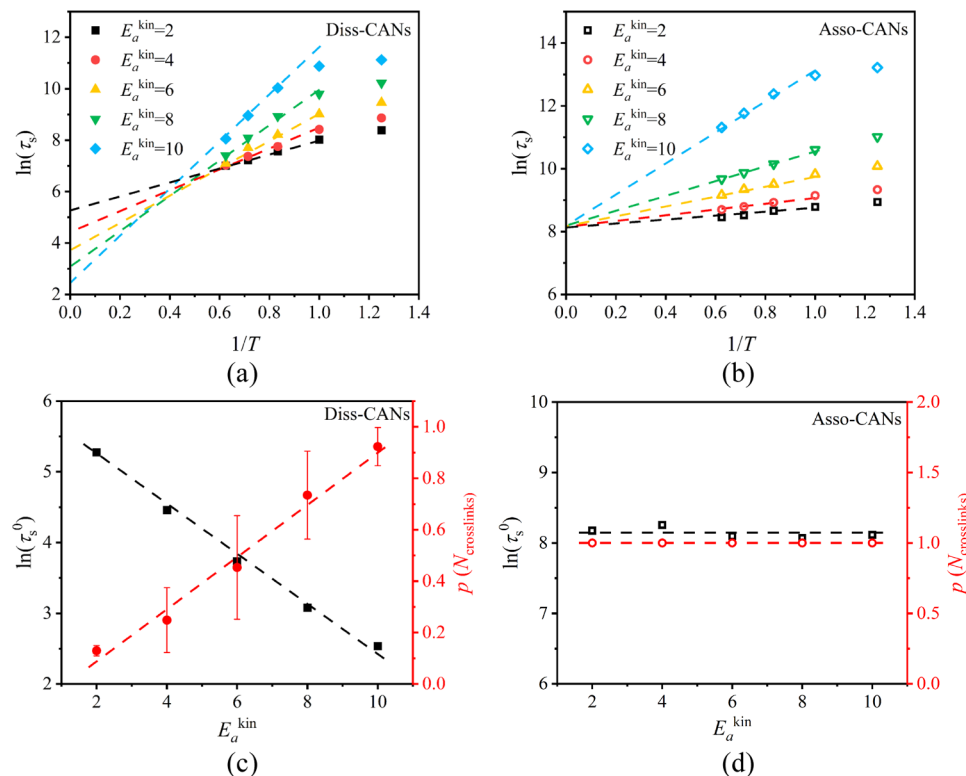
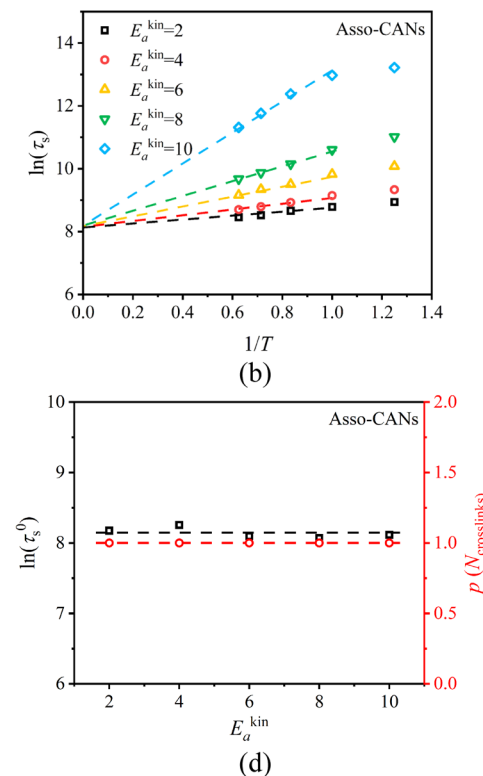


Figure 6. Terminal relaxation time τ_s as a function of $1/T$ for Diss-CANs (a) and Asso-CANs (b) and its prefactor τ_s^0 as a function of E_a^{kin} for Diss-CANs (c) and Asso-CANs (d). Dashed lines in (a) and (b) are fitted by eq 13. Symbols ● and ○ represent the fractions of existing cross-links for Diss-CANs (c) and Asso-CANs (d), respectively.

An interesting phenomenon is that all extended lines of τ_s meet at one intercept for Asso-CANs, namely, the same $\ln(\tau_s^0)$. For Diss-CANs, however, $\ln(\tau_s^0)$ decreases with increasing E_a^{kin} . This discrepancy can be attributed to the change of cross-linking density. As shown in Figures 6c,d, the fraction of existing cross-links $p(N_{\text{crosslinks}})$ for Dis-CANs increases with E_a^{kin} , which is in the opposite trend of $\ln(\tau_s^0)$, pointing to a negative correlation between τ_s^0 and $p(N_{\text{crosslinks}})$. Such a phenomenon is also observed in the experiment reported by Chen et al.⁵¹ The physical significance of τ_s^0 defined by Rubinstein is the characteristic time when a sticker diffuses the distance of its own size in the absence of any attraction from other stickers.⁹ Therefore, τ_s^0 is related to Rouse relaxation rather than the chemical reaction or network relaxation. With more connectivity of stickers, τ_s^0 may be severalfold than Rouse segment time τ_0 . As T increases, sticker dissociation additionally accelerates the relaxation of the network for Diss-CANs, leading to smaller τ_s . When $T \rightarrow \infty$, $\tau_s = \tau_s^0$, stickers completely dissociate, and, thus, the network formed by the chemical reaction between stickers no longer exists. The more the cross-links at lower T values, the more the loss of cross-links at $T \rightarrow \infty$. Therefore, the relaxation contributed by the loss of cross-links become faster, resulting in the decrease of τ_s^0 . Besides, if the cross-linking density is high, sticker movement will be hindered and the conformational entropy will be low. When the network disappears at $T \rightarrow \infty$, the lower the entropy, the faster the diffusion of stickers, namely, a smaller τ_s^0 .

On the other hand, instead of the disappearance of the network, the BERs just speed up for Asso-CANs at $T \rightarrow \infty$ because the reaction probability reaches unity. The reaction rate is completely controlled by prefactor A in eq 6, which is



related to p_{sc} . In other words, at this time, BERs will definitely occur and τ_s^0 depends on how quickly a bonded pair of stickers meet the other pair. Thus, a higher cross-linking density increases the probability and produces a smaller τ_s^0 for Asso-CANs. In our simulation, because of the conservative cross-links, τ_s^0 does not change with E_a^{kin} , as shown in Figure 6d.

In spite of the intricacy, we believe that, other than the temperature dependence of plateau modulus and viscosity, τ_s^0 is another way to distinguish the two CANs in terms of LVE.

4. NONLINEAR VISCOELASTICITY

As mentioned in Section 1, the difficulty in distinguishing the two kinds of networks in LVE relies on the change of cross-linking density. Although τ_s^0 can be seen as a criterion, it is not practical enough, especially for some networks with a narrow temperature range, which leads us to focus on nonlinear viscoelasticity. In addition, the application of CANs, like self-healing coatings⁴⁵ and rheology modifiers,⁵² also strongly requires the extension of the research from linear to nonlinear viscoelasticity. Therefore, by analogizing entangled polymers, we simulate CANs under steady and transient shear, and the results show that Diss-CANs and Asso-CANs have significant differences nonlinearly. More importantly, the upper and lower limits under an external field are detected.

4.1. Steady Shear. Steady shear is set for the two networks under different shear rates, which is shown in Figure 7; the

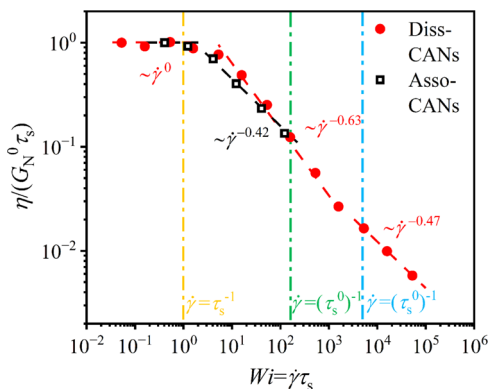


Figure 7. Shear thinning of Diss-CANs (●) and Asso-CANs (□). The steady viscosity is normalized by G_N^0 and τ_s . Dot-dashed lines represent the characteristic shear rates for Diss-CANs (yellow τ_s^{-1} and blue $(\tau_s^0)^{-1}$) and Asso-CANs (yellow τ_s^{-1} and green $(\tau_s^0)^{-1}$).

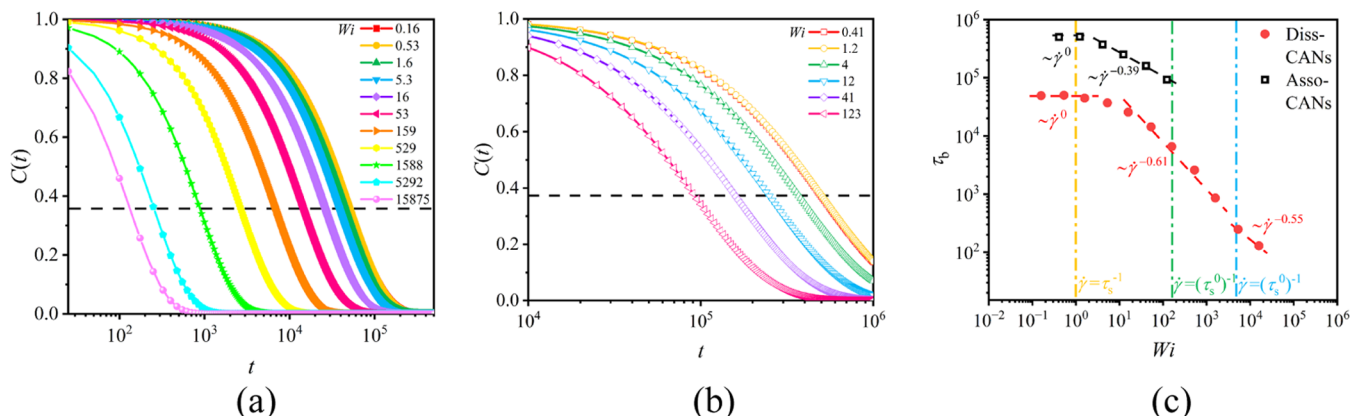


Figure 8. Autocorrelation function of the sticky bond $C(t)$ in eq 14 for Diss-CANs (a) and Asso-CANs (b) at different Wi and their lifetime (c). Black dashed lines in (a) and (b) refer to the attenuation of $C(t)$ to $1/e$.

steady viscosity $\eta/(G_N^0 \tau_s)$ is normalized as a function of Weissenberg number $Wi = \dot{\gamma} \tau_s$. All data are obtained over a long period of time to ensure a steady state is reached. As we can see, Diss-CANs have three scaling relationships in a much wider range of Wi , while Asso-CANs have only two.

For Diss-CANs, when $Wi < 1 (\dot{\gamma} < \tau_s^{-1})$, the steady shear is in the upper Newtonian region, where $\eta = \eta_0 \approx G_N^0 \tau_s$ (η_0 is the zero shear viscosity), irrelative to Wi . When $1 < Wi < 4800 (\tau_s^{-1} < \dot{\gamma} < (\tau_s^0)^{-1})$, where τ_s^0 is the prefactor of terminal relaxation time τ_s as mentioned above in LVE), stickers begin dissociating and $\eta \sim \dot{\gamma}^{-0.63}$. When $Wi > 4800 (\dot{\gamma} > (\tau_s^0)^{-1})$, shear thinning slows down and $\eta \sim \dot{\gamma}^{-0.47}$. In this region, the shear rate is too high (the chain does not have sufficient relaxation time) that stickers can rarely dissociate. In other words, most stickers should have been separated before the shear rate reaches $(\tau_s^0)^{-1}$ and the deceleration of thinning originates from the dominance of nonsticky friction. The index of -0.47 is close to those of entangled and unentangled linear polymers reported by Krogér.⁵³

Similarly, when $Wi < 1 (\dot{\gamma} < \tau_s^{-1})$, η values of Asso-CANs do not change with Wi and equal its η_0 . When $1 < Wi < 153 (\tau_s^{-1} < \dot{\gamma} < (\tau_s^0)^{-1})$, bond exchange reactions accelerate and the thinning begins. The scaling relationship is $\eta \sim \dot{\gamma}^{-0.42}$, which is smaller than Diss-CANs. When $Wi > 153 (\dot{\gamma} > (\tau_s^0)^{-1})$, the network can hardly be sheared because stickers of Asso-CANs are set without dissociation in the simulation, causing a significant reduction of the shear rate range. However, unlike simulations, we speculate that Asso-CANs with small E_a^{kin} can still be sheared when $\dot{\gamma} > (\tau_s^0)^{-1}$ in the experiments as a result of slight sticker dissociation, but this range of shear rates breaks the network, which should be avoided in the application scene of Asso-CANs.

Apparently, τ_s^0 is a key timescale that not only works in a linear regime but also decides the second transition and the upper limit shear rate of Diss-CANs and Asso-CANs, respectively. τ_s determines the lower limit of the critical shear rate at which shear thinning begins. Both τ_s^0 and τ_s are irrelative to the type of external field, reflecting the significance of multiscale relaxation time for nonlinear viscoelasticity. Note that $\tau_s^{-1} < \dot{\gamma} < (\tau_s^0)^{-1}$ is the whole range that Asso-CANs can withstand an external field nonlinearly. Therefore, for a better application of Asso-CANs, a moderately large cross-linking density is beneficial as the increasing cross-linking density contributes to longer τ_s and shorter τ_s^0 .

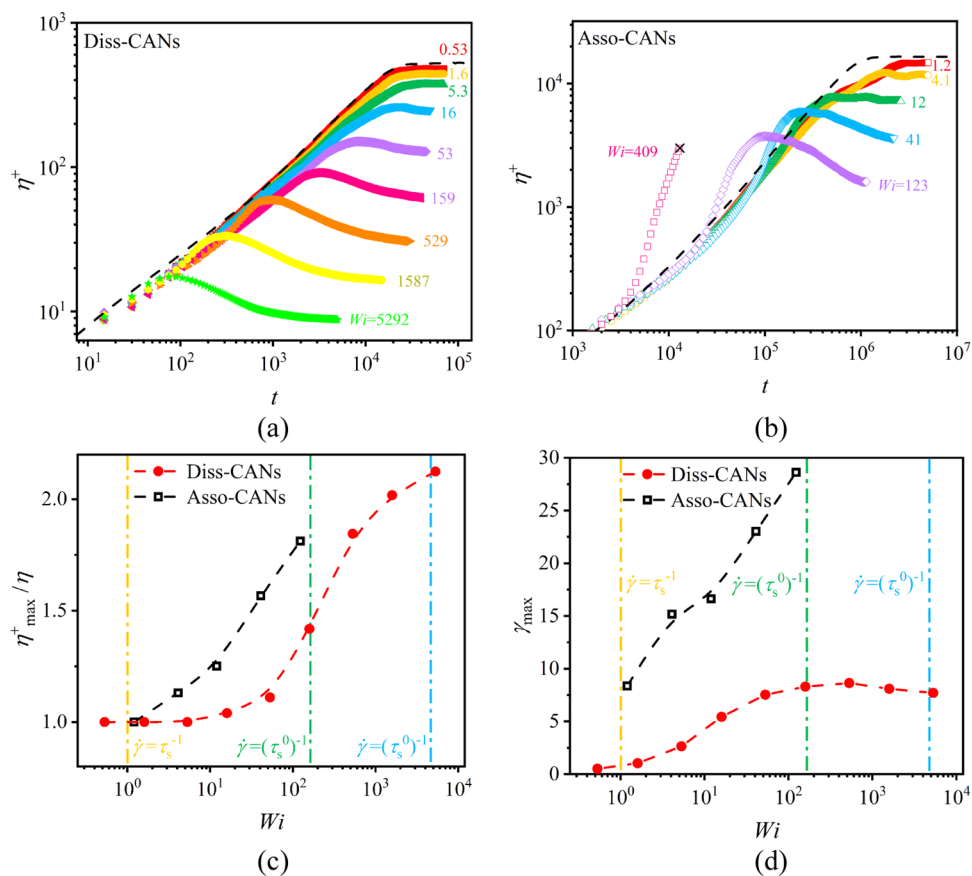


Figure 9. Shear rate start-up for Diss-CANs (a) and Asso-CANs (b) and plots of the ratio of the maximum of η^+ and steady shear viscosity η (c) and strain at stress maximum γ_{\max} (d) as a function of Wi . Black dashed lines in (a) and (b) are the LVE envelopes. Symbol \times in (b) represents the destruction of the network.

To better understand the network structure under shear, the lifetime of stickers is calculated using the decay of autocorrelation function $C(t)$ ^{16,17} defined as

$$C(t) = \frac{\langle H(t + \tau)H(t) \rangle}{\langle H(t)^2 \rangle} \quad (14)$$

where $H(t)$ is a bivariate function. If a pair of stickers are connected over an interval of τ , then $H(t) = 1$; otherwise, $H(t) = 0$. The values of the autocorrelation function $C(t)$ of Diss-CANs and Asso-CANs as a function of t at different Wi 's are shown in Figures 8a,b, respectively. As Wi increases, the chemical reactions speed up; therefore, $C(t)$ decays faster. By fitting it with the exponential function in the form of $C(t) = \exp(-t/\tau)$, the lifetime can be determined by $C(\tau_b) = 1/e$, where τ_b is the lifetime of stickers. The scaling relationship between τ_b and Wi , as shown in Figure 8c, is in accordance with that between viscosity and Wi in Figure 7, which demonstrates that sticker relaxation is a primary cause of shear thinning. The lifetime decreases slower when $\dot{\gamma} > (\tau_s^0)^{-1}$, proving again the deceleration of dissociation as mentioned above.

4.2. Shear Rate Start-Up. The shear stress growth coefficient $\eta^+ = \sigma(t)/\dot{\gamma}$ as a function of t at various shear rates under the shear rate start-up is plotted in Figure 9a,b, where $\sigma(t)$ is the shear stress. The black dashed lines are LVE envelopes calculated by the integral of $G(t)$. As the Wi (shear rate $\dot{\gamma}$) increases, both networks exhibit stress overshoot, but only Asso-CANs show obvious strain hardening. We calculate

the ratio of the maximum of η^+ and steady shear viscosity η in Figure 9c together with strain at stress maximum γ_{\max} in Figure 9d. The stress and strain growth of Asso-CANs is much faster than that of Diss-CANs. Interestingly, we find that γ_{\max} is close to $\ln(N_s^{1/2})$ for Diss-CANs at low Wi 's, as shown in Figure 9d, which is similar to $\ln(N_e^{1/2}) \approx 2$ (N_e is entangled length) of γ_{\max} in entangled polymers predicted by Doi and Edwards⁵⁴ for tube orientation in the absence of chain stretching. The maximum stretch ratio of APs can be defined as $\lambda_{\max} = N_s^{1/2}$, which depicts extending a random-coiled strand of size $N_s l$ to its limit $N_s l$, where l is the statistical bond length. Different from entangled polymers, it is N_s rather than N_e that decides λ_{\max} . For uniaxial elongation of a strand, the stretch ratio is $L(t)/L_0 = \exp(\dot{\epsilon}t)$, where $L(t)$ is the length of the sample at time t , L_0 is the original length, and $\dot{\epsilon}$ is the strain rate. When a strand is extended to $N_s l$, the maximum stretch ratio λ_{\max} is achieved, and the strain can be written as $\epsilon = \ln(N_s^{1/2})$, which demonstrates that, despite simple shear, the extension of a strand is still in accordance with uniaxial elongation as a result of the constraints of cross-links. Besides, the extension of a strand from $N_s^{1/2} l$ to $N_s l$ is dominated by alignment rather than stretching, suggesting that orientation is a major cause of stress overshoot at low Wi 's, which is the same as entangled polymers. Sticker dissociation leads to a slowdown of γ_{\max} at high Wi 's, as shown in Figure 9d. For Asso-CANs, on the contrary, the strain can be very large even at quite low Wi , as shown in Figure 9d, representative of weaker orientation.

Note that not all Wi 's in steady shear can be simulated under shear rate start-up. A smaller Wi causes an unstable numerical

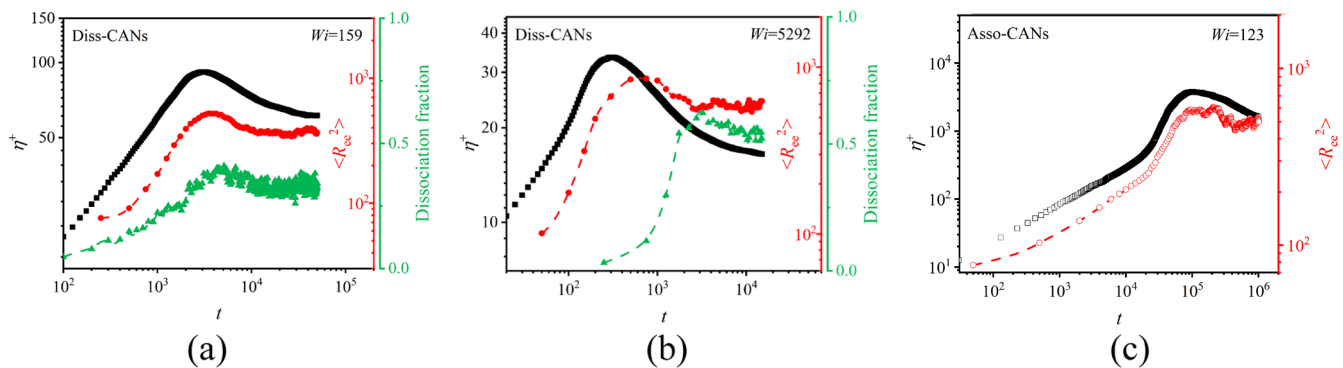


Figure 10. Comparison of η^+ (■ for Diss-CANs and □ for Asso-CANs) with $\langle R_{ee}^2 \rangle$ (● for Diss-CANs and ○ for Asso-CANs) and sticker dissociation fraction (▲) as a function of t under $Wi = 159$ (a) and under $Wi = 5292$ (b) for Diss-CANs and under $Wi = 123$ for Asso-CANs (c). Sticker dissociation fraction is not plotted in (c) because of the integrity of the network.

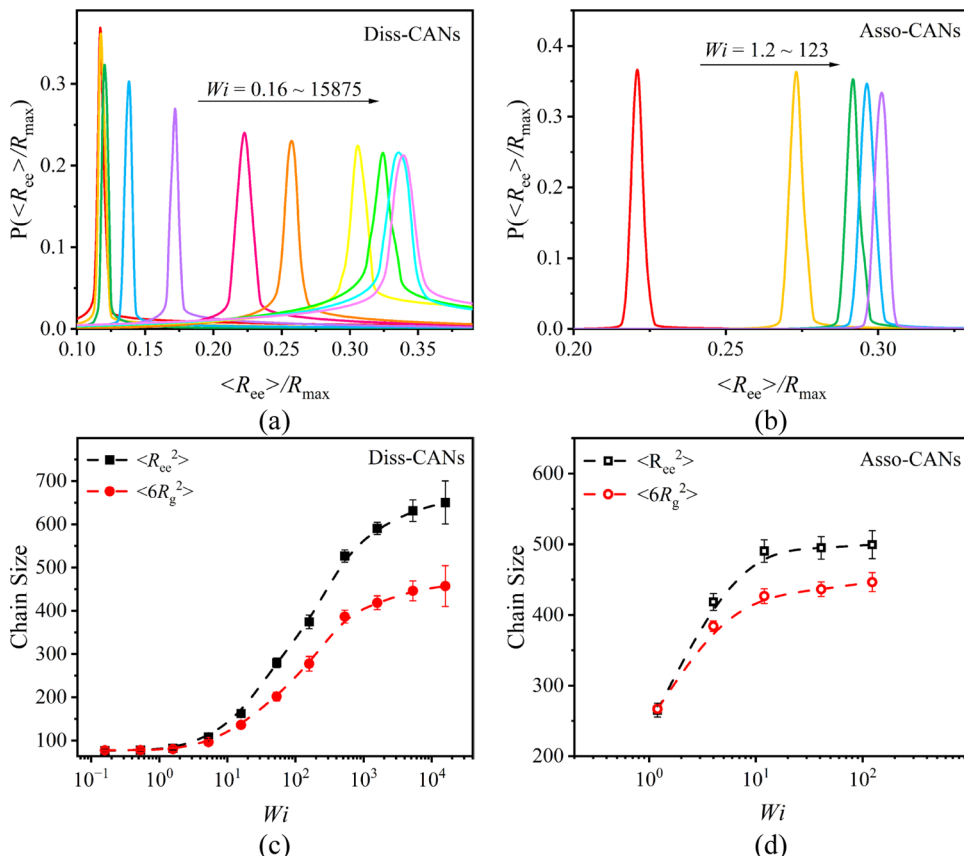


Figure 11. PDF of $\langle R_{ee}^2 \rangle / R_{max}$ at various Wi values for Diss-CANs (a) and Asso-CANs (b). Chain size as a function of Wi for Diss-CANs (c) and Asso-CANs (d). Symbols ■ and ● refer to $\langle R_{ee}^2 \rangle$ and $\langle 6R_g^2 \rangle$ for Diss-CANs, respectively. Symbols □ and ○ refer to $\langle R_{ee}^2 \rangle$ and $\langle 6R_g^2 \rangle$ for Asso-CANs, respectively.

value in the simulation ($Wi = 1.2$ and 4.1 of Asso-CANs can be two examples as they deviate from the LVE envelopes at a long time, as shown in Figure 9b, which also brings on the abnormality of γ_{max} , as shown in Figure 9d) and a higher Wi leads to a warning that FENE bonds are too long to hold the stickers together ($Wi = 409$ as an example for $\dot{\gamma} > (\tau_s^0)^{-1}$ and FENE bonds are ruptured at a short time). Therefore, a faster shear rate is only attained by step growth in steady shear, resulting incapability of shear rate start-up.

To investigate the network structure during shear rate start-up, we look into the change of chain conformation with time. The mean-squared end-to-end distance $\langle R_{ee}^2 \rangle$ and sticker

dissociation fraction of Diss-CANs are shown in Figure 10a,b, which also exhibit overshoot but with a lag compared with η^+ . As Wi grows, the lag increases. However, without dissociation, the $\langle R_{ee}^2 \rangle$ of Asso-CANs almost synchronizes with η^+ , as shown in Figure 10c. The lag of conformation behind η^+ can also be attributed to chain orientation, as discussed above in γ_{max} . Hence, shear thinning of Diss-CANs is actually a process of orientation-induced dissociation at $\dot{\gamma} < (\tau_s^0)^{-1}$, contributed by both chain orientation and sticker dissociation, whereas that of Asso-CANs is mainly controlled by BERs.

4.3. Tumbling of Diss-CANs. So far, we understand the essence of steady shear thinning, but the behavior that only

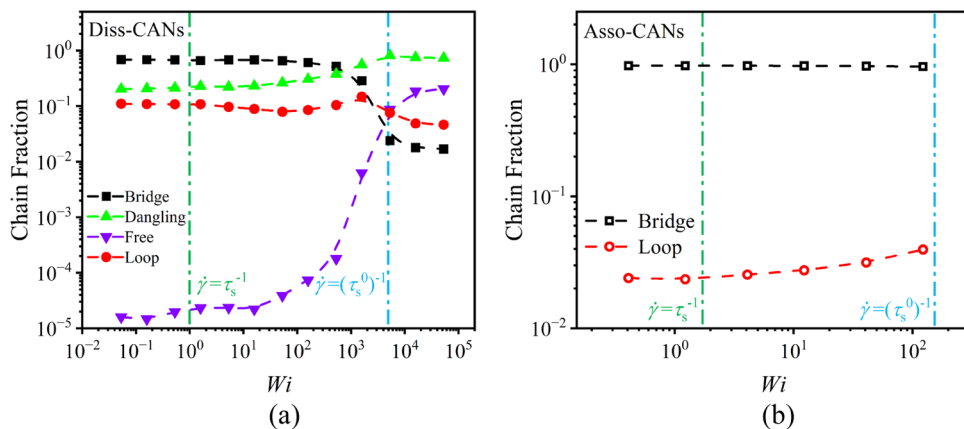


Figure 12. Change of the fraction of chain configuration types as a function of Wi for Diss-CANs (a) and Asso-CANs (b). Symbols ■, ●, ▲, and ▼ represent the bridge, loop, dangling, and free chains for Diss-CANs, respectively. Symbols □ and ○ represent the bridge and loop chains for Asso-CANs, respectively.

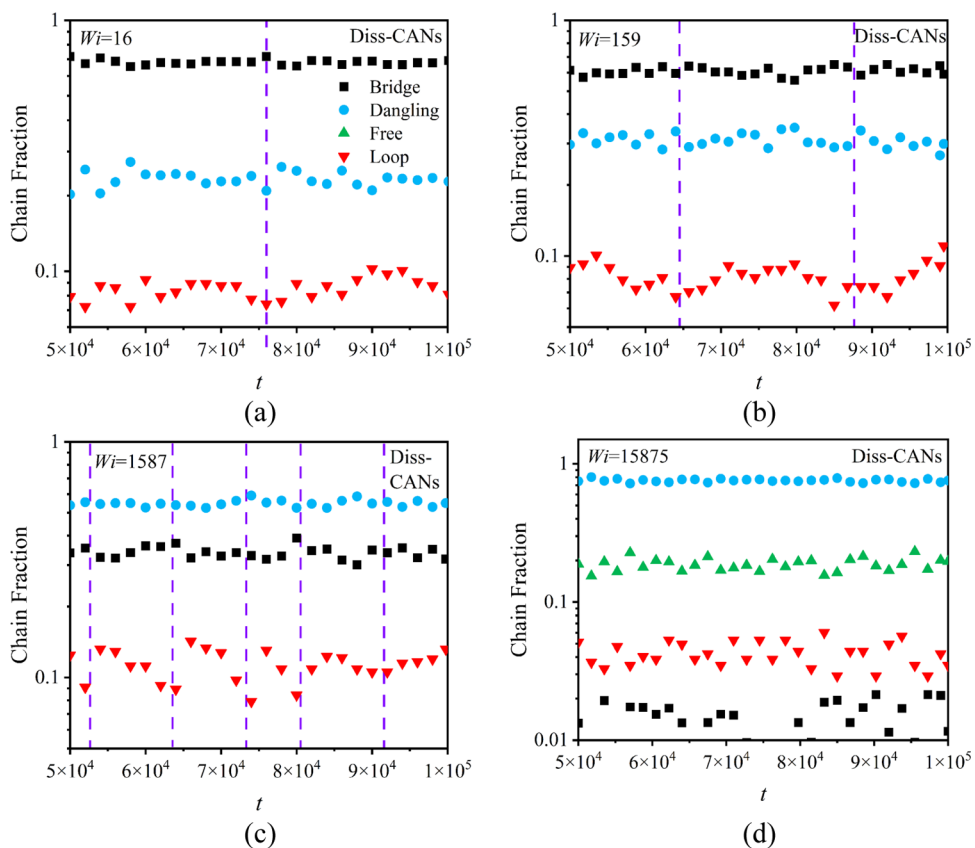


Figure 13. Change of the fraction of chain types with time for Diss-CANs under $Wi = 16$ (a), 159 (b), 1587 (c), and 15875 (d). Symbols ■, ●, ▼, and ▲ stand for the bridge, dangling, loop, and free chains, respectively. The purple dashed lines are the periods of tumbling.

Asso-CANs show strain hardening under transient shear is still unexplainable. According to the FENE model,^{55–60} strain hardening and shear thickening are related to non-Gaussian stretch, which means that some unknown effects weaken the FENE effect of Diss-CANs and result in the absence of strain hardening. As reported by Sefiddashti et al.,^{61–63} strong chain tumbling is found in entangled polymers at high Wi 's, which leads to disentanglements and the periodic change of molecular size. Inspired by their work, we analyze the tumbling behavior of the two networks.

The probability distribution function (PDF) of the normalized mean end-to-end distance $\langle R_{ee} \rangle / R_{\max}$ is discussed in Figure 11a,b, where R_{\max} is the theoretical fully extended chain end-to-end distance. As Wi grows, the peak shifts to larger values, demonstrating a shear-induced expansion of molecular size, which can be determined by $\langle R_{ee}^2 \rangle$ or $\langle 6R_g^2 \rangle$ (Figure 11c,d), either. The widened distribution illustrates the transition from Gaussian to non-Gaussian, also in agreement with the deviation between $\langle R_{ee}^2 \rangle$ and $\langle 6R_g^2 \rangle$ (Figures 11c,d). Compared with Asso-CANs, the conspicuous shifting and

widening for Diss-CANs support the argument that chain orientation plays an important role under transient shear.

Note that $\langle R_{ee}^2 \rangle \approx \langle R_g^2 \rangle$ is still workable at small Wi 's even for Diss-CANs, suggesting a random-coiled conformation of chains in a dynamic network. This is actually a core reason that APs are able to analogize entangled polymers,^{64,65} which also proves the rationality of describing the network with a single-Gaussian-chain model of SRM in our previous work.^{12,15} Furthermore, different from the multimodal distribution of molecular size at high Wi 's for entangled polymers, the non-Gaussian behavior is kept within a small range, indicating a hindrance from the network despite sticker dissociation.

PDF of $\langle R_{ee} \rangle / R_{max}$ disproves the tumbling behavior of both CANs that each chain undergoes periodic extension and collapse like entangled polymers, which strongly depends on the walking diffusion of stickers. However, hopping diffusion is predominant for APs, especially under the condition of strong association strength. Consequently, we further examine the tumbling behavior in the way of sticker hopping.

Diss-CANs consist of four different types of chain configurations: bridge, dangling, free, and loop chains, whereas Asso-CANs have only two: bridge and loop chains. Among them, only bridge chains can bear the stress and generate the FENE effect. The change of chain fraction as a function of Wi is plotted in Figure 12a,b. With fewer types of chains for Asso-CANs, the change is relatively simple, which only contains the transformation from the bridge to loop chains. For Diss-CANs, however, the situation is quite complicated. When $Wi < 1$ ($\dot{\gamma} < \tau_s^{-1}$) or $Wi > 4800$ ($\dot{\gamma} > (\tau_s^0)^{-1}$), chain fraction basically remains the same, which verifies the argument that sticker dissociation decreases dramatically at $\dot{\gamma} > (\tau_s^0)^{-1}$. In the region between τ_s^{-1} and $(\tau_s^0)^{-1}$, bridge chains are gradually converted into dangling and free chains.

The change of different chain types with time is also examined for Diss-CANs, as shown in Figure 13. To avoid the influence of start-up, data of $t > 50\,000$ are chosen. A periodic change can be seen before the shear rate reaches $(\tau_s^0)^{-1}$, and as Wi increases, the period shortens. Whenever bridge chains are at a maximum, the composition of dangling chains minimizes. This result agrees with the work of Sing et al.³⁵ When the network is stretched under shear, the sticker dissociates and forms dangling and free chains. The alignment of dangling and free chains with flow causes retractions, leading to the reformation of bridge chains. This is direct evidence of tumbling for APs under shear, demonstrating a periodic relaxation of stickers, which neutralizes the FENE effect. When $\dot{\gamma} > (\tau_s^0)^{-1}$, tumbling can no longer be observed as sticker dissociation is restrained, which implies that strain hardening should gradually start. Unfortunately, this shear rate is out of range for start-up in our simulation.

Note that we do not rule out other effects that attenuate strain hardening such as flow-induced friction reduction, reported by Matsumiya and Watanabe⁶⁶ and Bobbili and Milner.⁶⁷ We just consider tumbling as a dominant factor under shear. As reported by Huang,⁶⁸ their phenomenological model for entangled polymers under shear proves that flow-induced friction reduction without tumbling is not mighty enough to fit experimental data. The comparison of the two networks in this paper should be an excellent support to their work. Fewer chain types directly limit the tumbling of Asso-CANs, exhibiting a much more rigid network in nonlinear viscoelasticity.

Moreover, several figures in Section 4 show an inconspicuous transition in the region of $\tau_s^{-1} < \dot{\gamma} < (\tau_s^0)^{-1}$ for Diss-CANs, which is speculated to be a characteristic shear rate τ_R^{-1} , where τ_R is the Rouse time of the chain. When $\tau_s^{-1} < \dot{\gamma} < \tau_R^{-1}$, the network aligns with the flow and few stickers participate in dissociation. After τ_R^{-1} , more and more stickers dissociate and dominate shear thinning. In other words, there may exist a transition from orientation dominance to dissociation dominance, which can also be found in entangled polymers.^{61–63} As calculated through the fitting of SRM, the Rouse time of the chain is $\tau_R = 5758 \tau_{LJ}$ and corresponding $Wi = 9$. Because of weak orientation, this transition has a limited effect for Asso-CANs.

5. CONCLUSIONS

We have successfully simulated Diss-CANs and Asso-CANs in both EMD and NEMD using the hybrid MC/MD algorithm. Although the two networks behave similarly in LVE, a core discrepancy lies in the change of cross-linking density, which is reflected in the prefactor τ_s^0 of terminal relaxation time τ_s . For Diss-CANs, the cross-linking density increases with decreasing temperature and increasing kinetic activation energy, leading to the decrease of τ_s^0 as a result of the enhancement of sticker movements. On the contrary, τ_s^0 of Asso-CANs with conservative cross-links remains the same.

In nonlinear viscoelasticity, however, the differences become more apparent. On the one hand, compared with Diss-CANs, Asso-CANs can only withstand a small range of shear rates and have a weaker shear thinning behavior. On the other hand, only Asso-CANs exhibit strong strain hardening resulting from the FENE effect. The microstructure behind these macroscopic rheological phenomena is fascinating. For Diss-CANs, stickers dissociate under shear and bridge chains are converted into dangling and free chains, which can be easily aligned with the flow. The combined action of sticker dissociation and chain orientation leads to stronger shear thinning. Besides, the transformation between different types of chains is time-dependent. The retraction of oriented dangling and free chains in turn generates new bridge chains, forming a periodic cycle of tumbling, which weakens strain hardening. However, without dissociation, there are only bridge and loop chains for Asso-CANs, which take the edge off orientation and tumbling, showing a rigid network under shear.

Another important result is that our work presents a clear limit in the nonlinear application of APs, especially for Asso-CANs. When $\dot{\gamma} > (\tau_s^0)^{-1}$, chemical reactions are no longer in existence and the dynamic networks look the same as fixed networks. Therefore, $(\tau_s^0)^{-1}$ is an upper limit shear rate for Asso-CANs and some other APs with extremely high association strength. In conclusion, the present work reveals the differences between Diss-CANs and Asso-CANs in terms of both linear and nonlinear viscoelasticities and defines their usable range in the application scene.

AUTHOR INFORMATION

Corresponding Author

Ping Tang – State Key Laboratory of Molecular Engineering of Polymers, Department of Macromolecular Science, Fudan University, Shanghai 200433, China;  orcid.org/0000-0003-0253-1836; Email: pingtang@fudan.edu.cn

Authors

Xiang Cui – State Key Laboratory of Molecular Engineering of Polymers, Department of Macromolecular Science, Fudan University, Shanghai 200433, China

Nuofei Jiang – State Key Laboratory of Molecular Engineering of Polymers, Department of Macromolecular Science, Fudan University, Shanghai 200433, China

Jingyu Shao – State Key Laboratory of Molecular Engineering of Polymers, Department of Macromolecular Science, Fudan University, Shanghai 200433, China

Hongdong Zhang – State Key Laboratory of Molecular Engineering of Polymers, Department of Macromolecular Science, Fudan University, Shanghai 200433, China

Yuliang Yang – State Key Laboratory of Molecular Engineering of Polymers, Department of Macromolecular Science, Fudan University, Shanghai 200433, China

Complete contact information is available at:

<https://pubs.acs.org/10.1021/acs.macromol.2c02122>

Notes

The authors declare no competing financial interest.

ACKNOWLEDGMENTS

The authors thank the financial support from the National Natural Science Foundation of China (grant nos. 21973017, 21774027, and 21534002).

REFERENCES

- (1) Liu, K.; Kang, Y.; Wang, Z.; Zhang, X. 25th anniversary article: reversible and adaptive functional supramolecular materials: "non-covalent interaction" matters. *Adv. Mater.* **2013**, *25*, 5530–5548.
- (2) Miyamae, K.; Nakahata, M.; Takashima, Y.; Harada, A. Self-Healing, Expansion-Contraction, and Shape-Memory Properties of a Preorganized Supramolecular Hydrogel through Host-Guest Interactions. *Angew. Chem., Int. Ed.* **2015**, *54*, 8984–8987.
- (3) Lewis, C. L.; Dell, E. M. A review of shape memory polymers bearing reversible binding groups. *J. Polym. Sci., Part B: Polym. Phys.* **2016**, *54*, 1340–1364.
- (4) Jing, B. B.; Evans, C. M. Catalyst-Free Dynamic Networks for Recyclable, Self-Healing Solid Polymer Electrolytes. *J. Am. Chem. Soc.* **2019**, *141*, 18932–18937.
- (5) Lin, Y.; Chen, Y.; Yu, Z.; Huang, Z.; Lai, J.-C.; Tok, J. B. H.; Cui, Y.; Bao, Z. Reprocessable and Recyclable Polymer Network Electrolytes via Incorporation of Dynamic Covalent Bonds. *Chem. Mater.* **2022**, *34*, 2393–2399.
- (6) Denissen, W.; Winne, J. M.; Du Prez, F. E. Vitrimers: permanent organic networks with glass-like fluidity. *Chem. Sci.* **2016**, *7*, 30–38.
- (7) Montarnal, D.; Capelot, M.; Tournilhac, F.; Leibler, L. Silica-Like Malleable Materials from Permanent Organic Networks. *Science* **2011**, *334*, 965–968.
- (8) Hoy, R. S.; Fredrickson, G. H. Thermoreversible associating polymer networks. I. Interplay of thermodynamics, chemical kinetics, and polymer physics. *J. Chem. Phys.* **2009**, *131*, No. 224902.
- (9) Stukalin, E. B.; Cai, L.-H.; Kumar, N. A.; Leibler, L.; Rubinstein, M. Self-Healing of Unentangled Polymer Networks with Reversible Bonds. *Macromolecules* **2013**, *46*, 7525–7541.
- (10) Wu, S.; Yang, H.; Huang, S.; Chen, Q. Relationship between Reaction Kinetics and Chain Dynamics of Vitrimers Based on Dioxaborolane Metathesis. *Macromolecules* **2020**, *53*, 1180–1190.
- (11) Wu, S.; Yang, H.; Xu, W.-S.; Chen, Q. Thermodynamics and Reaction Kinetics of Symmetric Vitrimers Based on Dioxaborolane Metathesis. *Macromolecules* **2021**, *54*, 6799–6809.
- (12) Jiang, N.; Zhang, H.; Tang, P.; Yang, Y. Linear Viscoelasticity of Associative Polymers: Sticky Rouse Model and the Role of Bridges. *Macromolecules* **2020**, *53*, 3438–3451.
- (13) Jiang, N.; Zhang, H.; Yang, Y.; Tang, P. Molecular dynamics simulation of associative polymers: Understanding linear viscoelasticity from the sticky Rouse model. *J. Rheol.* **2021**, *65*, 527–547.
- (14) Ricarte, R. G.; Shanbhag, S. Unentangled Vitrimer Melts: Interplay between Chain Relaxation and Cross-link Exchange Controls Linear Rheology. *Macromolecules* **2021**, *54*, 3304–3320.
- (15) Shao, J.; Jiang, N.; Zhang, H.; Yang, Y.; Tang, P. Sticky Rouse Model and Molecular Dynamics Simulation for Dual Polymer Networks. *Macromolecules* **2022**, *55*, 535–549.
- (16) Wu, J. B.; Li, S. J.; Liu, H.; Qian, H. J.; Lu, Z. Y. Dynamics and reaction kinetics of coarse-grained bulk vitrimers: a molecular dynamics study. *Phys. Chem. Chem. Phys.* **2019**, *21*, 13258–13267.
- (17) Perego, A.; Khabaz, F. Volumetric and Rheological Properties of Vitrimers: A Hybrid Molecular Dynamics and Monte Carlo Simulation Study. *Macromolecules* **2020**, *53*, 8406–8416.
- (18) Perego, A.; Lazarenko, D.; Cloitre, M.; Khabaz, F. Microscopic Dynamics and Viscoelasticity of Vitrimers. *Macromolecules* **2022**, *55*, 7605–7613.
- (19) Rao, A.; Ramirez, J.; Olsen, B. D. Mechanisms of Self-Diffusion of Linear Associative Polymers Studied by Brownian Dynamics Simulation. *Macromolecules* **2021**, *54*, 11212–11227.
- (20) Elling, B. R.; Dichtel, W. R. Reprocessable Cross-Linked Polymer Networks: Are Associative Exchange Mechanisms Desirable? *ACS Cent. Sci.* **2020**, *6*, 1488–1496.
- (21) Jourdain, A.; Asbai, R.; Anaya, O.; Chehimi, M. M.; Drockenmuller, E.; Montarnal, D. Rheological Properties of Covalent Adaptable Networks with 1,2,3-Triazolium Cross-Links: The Missing Link between Vitrimers and Dissociative Networks. *Macromolecules* **2020**, *53*, 1884–1900.
- (22) Porath, L. E.; Evans, C. M. Importance of Broad Temperature Windows and Multiple Rheological Approaches for Probing Viscoelasticity and Entropic Elasticity in Vitrimers. *Macromolecules* **2021**, *54*, 4782–4791.
- (23) Chen, Q.; Zhang, Z.; Colby, R. H. Viscoelasticity of entangled random polystyrene ionomers. *J. Rheol.* **2016**, *60*, 1031–1040.
- (24) Huang, C.; Chen, Q.; Weiss, R. A. Nonlinear Rheology of Random Sulfonated Polystyrene Ionomers: The Role of the Sol–Gel Transition. *Macromolecules* **2016**, *49*, 9203–9214.
- (25) Shabbir, A.; Huang, Q.; Baeza, G. P.; Vlassopoulos, D.; Chen, Q.; Colby, R. H.; Alvarez, N. J.; Hassager, O. Nonlinear shear and uniaxial extensional rheology of polyether-ester-sulfonate copolymer ionomer melts. *J. Rheol.* **2017**, *61*, 1279–1289.
- (26) Zhang, Z.; Huang, C.; Weiss, R. A.; Chen, Q. Association energy in strongly associative polymers. *J. Rheol.* **2017**, *61*, 1199–1207.
- (27) Wu, S.; Cao, X.; Zhang, Z.; Chen, Q.; Matsumiya, Y.; Watanabe, H. Molecular Design of Highly Stretchable Ionomers. *Macromolecules* **2018**, *51*, 4735–4746.
- (28) Liu, S.; Zhang, Z.; Chen, Q.; Matsumiya, Y.; Watanabe, H. Nonlinear Rheology of Telechelic Ionomers Based on Sodium Sulfonate and Carboxylate. *Macromolecules* **2021**, *54*, 9724–9738.
- (29) Yang, H.; Wu, S.; Chen, Q. How to Choose a Secondary Interaction to Improve Stretchability of Associative Polymers? *Macromolecules* **2021**, *54*, 8112–8121.
- (30) Liu, S.; Zhang, Y.; Zhang, Z.; Chen, Q. Nonlinear rheological behavior of telechelic ionomers with the distribution of ionic stickers at the ends. *J. Rheol.* **2022**, *66*, 1–16.
- (31) Zhang, Z.; Liu, C.; Cao, X.; Gao, L.; Chen, Q. Linear Viscoelastic and Dielectric Properties of Strongly Hydrogen-Bonded Polymers near the Sol–Gel Transition. *Macromolecules* **2016**, *49*, 9192–9202.
- (32) Suzuki, S.; Uneyama, T.; Inoue, T.; Watanabe, H. Nonlinear Rheology of Telechelic Associative Polymer Networks: Shear Thinning and Thinning Behavior of Hydrophobically Modified Ethoxylated Urethane (HEUR) in Aqueous Solution. *Macromolecules* **2012**, *45*, 888–898.
- (33) Uneyama, T.; Suzuki, S.; Watanabe, H. Concentration dependence of rheological properties of telechelic associative polymer solutions. *Phys. Rev. E* **2012**, *86*, No. 031802.

- (34) Suzuki, S.; Uneyama, T.; Watanabe, H. Concentration Dependence of Nonlinear Rheological Properties of Hydrophobically Modified Ethoxylated Urethane Aqueous Solutions. *Macromolecules* **2013**, *46*, 3497–3504.
- (35) Sing, M. K.; Wang, Z. G.; McKinley, G. H.; Olsen, B. D. Celebrating Soft Matter's 10th Anniversary: chain configuration and rate-dependent mechanical properties in transient networks. *Soft Matter* **2015**, *11*, 2085–2096.
- (36) Amin, D.; Wang, Z. Nonlinear rheology and dynamics of supramolecular polymer networks formed by associative telechelic chains under shear and extensional flows. *J. Rheol.* **2020**, *64*, 581–600.
- (37) Everaers, R.; Sukumaran, S. K.; Grest, G. S.; Svaneborg, C.; Sivasubramanian, A.; Kremer, K. Rheology and microscopic topology of entangled polymeric liquids. *Science* **2004**, *303*, 823–826.
- (38) Hoy, R. S.; Foteinopoulou, K.; Kroger, M. Topological analysis of polymeric melts: chain-length effects and fast-converging estimators for entanglement length. *Phys. Rev. E* **2009**, *80*, No. 031803.
- (39) Amin, D.; Likhtman, A. E.; Wang, Z. Dynamics in Supramolecular Polymer Networks Formed by Associating Telechelic Chains. *Macromolecules* **2016**, *49*, 7510–7524.
- (40) Manousiouthakis, V. I.; Deem, M. W. Strict detailed balance is unnecessary in Monte Carlo simulation. *J. Chem. Phys.* **1999**, *110*, 2753–2756.
- (41) Sciortino, F. Three-body potential for simulating bond swaps in molecular dynamics. *Eur. Phys. J. E: Soft Matter* **2017**, *40*, No. 3.
- (42) Ciarella, S.; Sciortino, F.; Ellenbroek, W. G. Dynamics of Vitrimers: Defects as a Highway to Stress Relaxation. *Phys. Rev. Lett.* **2018**, *121*, No. 058003.
- (43) Ciarella, S.; Biezemans, R. A.; Janssen, L. M. C. Understanding, predicting, and tuning the fragility of vitrimeric polymers. *Proc. Natl. Acad. Sci. U.S.A.* **2019**, *116*, 25013–25022.
- (44) Rovigatti, L.; Nava, G.; Bellini, T.; Sciortino, F. Self-Dynamics and Collective Swap-Driven Dynamics in a Particle Model for Vitrimers. *Macromolecules* **2018**, *51*, 1232–1241.
- (45) Ciarella, S.; Ellenbroek, W. Swap-Driven Self-Adhesion and Healing of Vitrimers. *Coatings* **2019**, *9*, 114.
- (46) Baig, C.; Edwards, B. J.; Keffer, D. J.; Cochran, H. D. A proper approach for nonequilibrium molecular dynamics simulations of planar elongational flow. *J. Chem. Phys.* **2005**, *122*, No. 114103.
- (47) Edwards, B. J.; Baig, C.; Keffer, D. J. A validation of the p-SLLOD equations of motion for homogeneous steady-state flows. *J. Chem. Phys.* **2006**, *124*, No. 194104.
- (48) Green, M. S. Markoff Random Processes and the Statistical Mechanics of Time-Dependent Phenomena. II. Irreversible Processes in Fluids. *J. Chem. Phys.* **1954**, *22*, 398–413.
- (49) Kubo, R. Statistical-Mechanical Theory of Irreversible Processes. I. General Theory and Simple Applications to Magnetic and Conduction Problems. *J. Phys. Soc. Jpn.* **1957**, *12*, 570–586.
- (50) Ramírez, J.; Sukumaran, S. K.; Vorselaars, B.; Likhtman, A. E. Efficient on the fly calculation of time correlation functions in computer simulations. *J. Chem. Phys.* **2010**, *133*, No. 154103.
- (51) Chen, M.; Si, H.; Zhang, H.; Zhou, L.; Wu, Y.; Song, L.; Kang, M.; Zhao, X.-L. The Crucial Role in Controlling the Dynamic Properties of Polyester-Based Epoxy Vitrimers: The Density of Exchangeable Ester Bonds (v). *Macromolecules* **2021**, *54*, 10110–10117.
- (52) He, C.; Christensen, P. R.; Seguin, T. J.; Wood, B. M.; Persson, K. A.; Russell, T. P.; Helms, B. A.; et al. Conformational Entropy as a Means to Control the Behavior of Poly(diketonenamine) Vitrimers In and Out of Equilibrium. *Angew. Chem., Int. Ed.* **2020**, *59*, 735–739.
- (53) Kröger, M.; Hess, S. Rheological Evidence for a Dynamical Crossover in Polymer Melts via Nonequilibrium Molecular Dynamics. *Phys. Rev. Lett.* **2000**, *85*, 1128–1131.
- (54) Doi, M. *The Theory of Polymer Dynamics*; Clarendon Press, 1986; pp 255–268.
- (55) Warner, H. R., Jr. Kinetic Theory and Rheology of Dilute Suspensions of finitely extensible dumbbells. *Ind. Eng. Chem. Fundam.* **1972**, *11*, 379–387.
- (56) Bird, R. B.; Curtiss, C. F.; Armstrong, R. C.; Hassager, O. *Dynamics of polymeric liquids Vol 2 Kinetic Theory*; John Wiley & Sons Inc, 1989; pp 76–85.
- (57) Watanabe, H. Viscoelasticity and dynamics of entangled polymers. *Prog. Polym. Sci.* **1999**, *24*, 1253–1403.
- (58) McLeish, T. C. B. Tube theory of entangled polymer dynamics. *Adv. Phys.* **2002**, *51*, 1379–1527.
- (59) Larson, R. G.; Desai, P. S. Modeling the Rheology of Polymer Melts and Solutions. *Annu. Rev. Fluid Mech.* **2015**, *47*, 47–65.
- (60) Watanabe, H.; Matsumiya, Y.; Sato, T. Revisiting Nonlinear Flow Behavior of Rouse Chain: Roles of FENE, Friction-Reduction, and Brownian Force Intensity Variation. *Macromolecules* **2021**, *54*, 3700–3715.
- (61) Nafar Sefiddashti, M. H.; Edwards, B. J.; Khomami, B. Individual chain dynamics of a polyethylene melt undergoing steady shear flow. *J. Rheol.* **2015**, *59*, 119–153.
- (62) Nafar Sefiddashti, M. H.; Edwards, B. J.; Khomami, B. Evaluation of reptation-based modeling of entangled polymeric fluids including chain rotation via nonequilibrium molecular dynamics simulation. *Phys. Rev. Fluids* **2017**, *2*, No. 083301.
- (63) Nafar Sefiddashti, M. H.; Edwards, B. J.; Khomami, B. Individual Molecular Dynamics of an Entangled Polyethylene Melt Undergoing Steady Shear Flow: Steady-State and Transient Dynamics. *Polymers* **2019**, *11*, 476.
- (64) Groot, R. D.; Agterof, W. G. M. Dynamic viscoelastic modulus of associative polymer networks: Off-lattice simulations, theory and comparison to experiments. *Macromolecules* **1995**, *28*, 6284–6295.
- (65) Wientjes, R. H. W.; Jongschaap, R. J. J.; Duits, M. H. G.; Mellema, J. A new transient network model for associative polymer networks. *J. Rheol.* **1999**, *43*, 375–391.
- (66) Matsumiya, Y.; Watanabe, H.; Masubuchi, Y.; Huang, Q.; Hassager, O. Nonlinear Elongational Rheology of Unentangled Polystyrene and Poly(p-tert-butylstyrene) Melts. *Macromolecules* **2018**, *51*, 9710–9729.
- (67) Bobbili, S. V.; Milner, S. T. Chain tension reduces monomer friction in simulated polymer melts. *J. Rheol.* **2020**, *64*, 1373–1378.
- (68) Costanzo, S.; Huang, Q.; Ianniruberto, G.; Marrucci, G.; Hassager, O.; Vlassopoulos, D. Shear and Extensional Rheology of Polystyrene Melts and Solutions with the Same Number of Entanglements. *Macromolecules* **2016**, *49*, 3925–3935.